Fuel 403 (2026) 136094

Contents lists available at ScienceDirect

Fuel

journal homepage: www.elsevier.com/locate/jfue

Full length article

Analyzing iron dust bunsen flames using numerical simulations

T. Hazenberg [a,*], D. Braig [a], M.A. Fedoryk [b], J. Mich [a], F.P. Hagen [b], S.R. Harth [b], B. Stelzner [b], A. Scholtissek [a], D. Trimis [b], C. Hasse [a]

[a] Technical University of Darmstadt, Department of Mechanical Engineering, Simulation of reactive Thermo-Fluid Systems, Otto-Berndt-Straße 2, 64287 Darmstadt, Germany

[b] Engler-Bunte-Institute, Combustion Technology, Karlsruhe Institute of Technology, Engler-Bunte-Ring 7, 76131 Karlsruhe, Germany

HIGHLIGHTS

- 3D simulations of iron dust Bunsen flame.
- Extracted laminar burner velocity compared to idealized 1D flame simulation and experimental result.
- Best-to-date experimental validation of iron dust flame model.
- Distinct differences between idealized 1D flame and Bunsen setup identified.

ARTICLE INFO

Keywords:
Metal fuels
Bunsen flame
Iron dust combustion
Validation
Burning velocity

ABSTRACT

This article presents numerical simulations of an iron dust Bunsen flame. The results are validated against experimental results. The burning velocity is extracted from the 3D simulation results, as in the experiments. The agreement of the burning velocity between the model and experiment is one of the best-to-date for iron dust flames. A comparison is performed between 3D and 1D simulations to improve our understanding of how the 3D Bunsen flame deviates from an ideal 1D flame. This comparison reveals that the co-flow mixes with the post-flame zone, increasing the oxygen concentration in the reaction layer, which increases the burning velocity. Moreover, the analysis also reveals that stretch and curvature affect the burning velocity. These results are valuable for the future development of experimental setups aimed at measuring the burning velocity.

1. Introduction

Moving away from fossil fuels to renewable energy sources provides several challenges. One of these is introducing intermittent renewable energy sources, i.e., solar and wind, to the electricity grid while maintaining stable operation. Renewable chemical energy carriers then become a requirement for temporary energy storage. These can account for load fluctuations or transport energy from regions with high to low renewable energy potential. An interesting category of carbon-free energy carriers, which has received increased attention lately, is metals, e.g., [1–3]. Metal powders can be used to operate a carbon-free energy cycle. First, the metal powder is combusted, releasing energy, and the combustion product is metal oxides. The metal oxides are captured and reduced with green hydrogen (energy storage), returning the metal oxide to metal and closing the cycle. A promising candidate for constructing such a metal-based energy cycle is iron, which is the focus of this work.

Compared to other solid fuels, like coal and biomass, research on iron powders for energy storage and supply is still in its infancy. A lot of pioneering work on iron (and other metal fuels for heat and power supply) has been performed at McGill University in Canada, e.g., [4]. Iron powder can be rapidly oxidized with air in iron dust flames, releasing the stored energy as heat. However, the operation of iron dust flames is non-trivial since several fundamental differences exist between such (non-volatile) solid fuel flames, and conventional gas flames as pointed out by Goroshin et al. [4]. Among others, the particle temperature can significantly exceed the gas temperature; fuel and oxidizer concentration relate non-trivially as the fuel does not diffuse, and the flame structure becomes distorted due to the particles' thermal

* Corresponding author.
Email address: hazenberg@stfs.tu-darmstadt.de (T. Hazenberg).

https://doi.org/10.1016/j.fuel.2025.136094
Received 31 March 2025; Received in revised form 25 May 2025; Accepted 22 June 2025
Available online 28 June 2025

inertia [5]. Consequently, the burning velocity and temperature respond differently to the fuel–oxygen equivalence ratio than gas flames [6]. In the past, iron dust flames have been established experimentally in various configurations, such as counterflow flames [7], methane/iron hybrid Bunsen flames [8], conventional Bunsen-type flames [9], spherical flames [10,11], methane/iron hybrid flat flame burners [12], lifted flames [13], and top-fired swirled tornado flames [14]. Even though several stable flames could be operated in the lab, important flame characteristics, such as the flame stabilization mechanisms, are not thoroughly understood and warrant further research.

Parallel to the experimental work, significant progress has been made in the model development of metal dust flames. In one of the earlier numerical works by Soo et al. [15], they developed a single-particle model and used this to investigate the transient propagation of a hypothetical dust flame. Later, Hazenberg and van Oijen [6] extended this model with temperature-dependent transport properties and based the particle model properties on those of iron. In their model, iron is modeled with constant heat capacity, and they modified the combustion enthalpy to obtain a consistent flame temperature. They then simulated the first 1D iron flames. After that work, several model variations and studies were performed using this model as a base. Van Gool et al. [16] extended the model with temperature-dependent thermodynamic properties for iron and considered oxidation to the highest oxidation state (Fe_2O_3). The utilized thermodynamic table was later improved by Mich et al. [17] by accounting for the mixing enthalpy and entropy of the L1/L2 liquid to capture the “reactive cooling” after peak particle temperature. The original model and variants (inspired by [16,18–20]) were used by Ravi et al. [21,22] and Mich et al. [23] to investigate the influence of particle size distributions. The first to explore 3D effects on a 1D flame was Van Gool et al. [24], who studied the impact of flame stretch using a 1D approximation to the counterflow setup. Until now, only two numerical studies of laminar flame propagation have been performed in 3D: 1) Wen et al. [25] they studied the counterflow setup of McRae et al. [7], and 2) Ramaekers et al. [26] they studied the impact of radiation on the tube flames of Tang et al. [27,28]. Rather differently, but not less useful, Vance et al. [29–31] have studied flame propagation using boundary layer resolved simulations, providing useful insights into the discrete regime [32–34].

It is generally accepted that the individual particles in an iron dust flame burn in the diffusion-limited regime, e.g., [4,6,15]. The combustion duration of a single particle burning in the diffusion-limited regime has been extensively validated using single-particle experiments [16,18,21,23,35,36]. In contrast, validation of the burning velocity for iron dust has not been challenging; the burning velocity predicted by 1D models is underpredicted by roughly a factor of two [6,26,27], which is attributed to the curved flame in the experiment [27]. The underprediction is surprising, as the diffusion-limited combustion, which has been validated, provides a clear upper limit on the mass burning rate and, thus, flame propagation velocity. To further substantiate the challenge, Mich et al. [23] have shown that the burning does not strongly depend on the choice of oxidation model. This raises the question: How can we reconcile a significant underprediction of the burning velocity while the community has shown to understand the combustion of individual particles? In other words, are we missing some significant physical effect, or do we not fully understand how to interpret the experiments?

Recently, Ramaekers et al. [26] took the first steps towards answering these questions. They performed 3D simulations of the experiments from Tang et al. [27,34] both with particle-to-particle radiation and without. The flames in the 3D simulations without particle-to-particle radiation did not propagate significantly faster than predicted by 1D models. However, the flame simulation with the finest powder reported by Tang et al., and with particle-to-particle radiation enabled, was significantly accelerated compared to 1D models. While the flames were not radiation-driven in the sense that particle-to-particle radiation is the main mechanism of flame propagation, they were enhanced by radiation. The significant flame speed enhancement was unexpected, as the setup diameter is only slightly larger than the optical path length in the unburned powder, meaning most radiation is lost to the environment. When Fedoryk et al. [9] presented their experimental results of iron dust flames on a Bunsen setup, 1D models again underpredicted the results (see Fig. 12 of this work). In this case, as the setup diameter (20 mm) is significantly less than the optical path length ($\mathcal{O}(100\ \text{mm})$, estimated from 20 % laser power [9]), particles-to-particle radiation can not explain the difference. Thus, we want to conduct 3D simulations of the Bunsen setup to improve our understanding. Improving our understanding of an academic setup like this is crucial for further model validation.

In this article, we will present 3D numerical simulations of the experimental Bunsen flame of Fedoryk et al. [9]. To this end, a point particle method in OpenFOAM® is utilized. The particle model is that by Hazenberg and van Oijen [6], with the thermodynamic properties and Stefan flow of Mich et al. [23]. As Mich et al. already validated the burn time of the particle model against experiments by Ning et al. [37], we will not repeat those results. A particle size distribution is utilized in the experiments, which we approximate with a log-hyperbolic distribution function [38]. Our goal is twofold: First and foremost, we would like to validate our numerical model for the iron dust Bunsen setup, and second, we would like to identify if the Bunsen flame can, locally, be approximated as a 1D flame. This article is split into several sections: first, we provide a short description of the experimental setup; second, the numerical model is introduced; third, the results are presented; fourth, a discussion on uncertainties and future work is provided; and finally, we give conclusions.

2. Experimental bunsen flame setup

The experimental setup utilizes iron powder of purity greater than 99.5 % (PMCtec GmbH, type YTF-HY2) as a fuel, which is contained in a cylindrical tube and shifted upwards by a piston connected to a stepper motor as shown in Fig. 1. The dispersion of the iron powder occurs in a so-called air-knife seeder in a small gap of approximately 30 μm height with high gas velocity. Mass flow controllers control the air mass flow in the seeder/burner and co-flow stream.

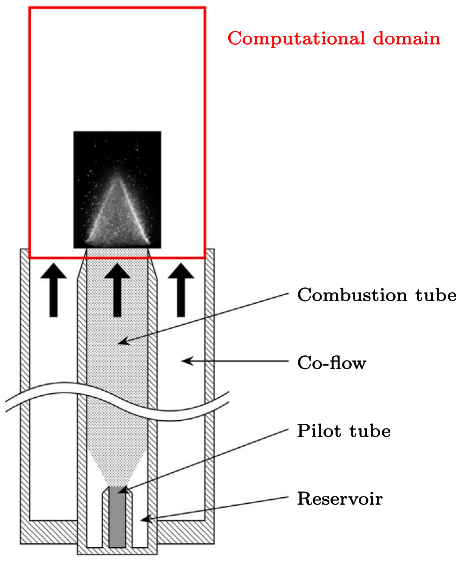

Fig. 1. Sketch of the experimental configuration presented by Fedoryk et al. [9]. Several of the relevant parts of the setup are indicated. The computational domain, which extends 8 cm above the combustion tube and co-flow outlet, is marked in red. A picture of the experimental flame, scaled correctly with respect to the computational domain, is inserted as a reference. (For interpretation of the references to colour in this figure legend, the reader is referred to the web version of this article.)

Fig. 1 further shows the burner setup, which consists of two concentric tubes: An inner pilot tube and an outer combustion tube with a diameter of 20.5 mm and length of 35 cm downstream from the pilot tube outlet. As the iron powder suspension exits the pilot tube, the flow slows down, causing some particles to fall. It has also been observed that a few particles can also stick to the wall of the larger combustion tube before dropping. The falling powder is collected in a separate reservoir, minimizing fluctuations in the particle seeding. The outlet tube of the burner is surrounded by a co-flow with a larger diameter to enhance flame stability and protect the flame from external influences. Both the co-flow and combustion air were supplied at room temperature. The mean inlet velocity of the co-flow and the combustion pipe are identical and can vary between 25 and 45 cm/s. A more detailed description can be found in Fedoryk et al. [9].

In the experiments the burning velocity is estimated using the following method. Using PIV the velocity profile at the outlet of the combustion tube is measured. It is found that this velocity profile is close to that of a fully developed pipe flow. As the particles burn brightly during combustion, the luminosity of the particles can be used to identify the flame front. Several photographs of the flame are taken, which are then averaged to obtain an averaged flame. As these photographs are a line-of-sight measurement of the flame, the Abel inverse is computed to get the radial profile of the flame. The position of the flame front is then identified by finding the innermost visible cone of light. To get an approximate surface of the flame, a fifth order polynomial is fitted to this inner cone. Finally, at every radial position the angle of this flame cone with respect to the upward direction is determined. The angle can then be used in conjunction with the PIV measured velocity profile at the inlet to determine the burning velocity at every radial position. To get the global burning velocity, the radial velocity is then averaged between 0.4 and 0.7 times the radius of the combustion tube.

3. Numerical methods

In the following, we present the framework for the numerical simulation of iron–air Bunsen flames. The governing equations include both gas and particulate phase modeling. After the governing equations, the relevant boundary conditions are introduced. Thereafter, details about the computational setup are provided.

3.1. Euler–Lagrange framework

The iron–air Bunsen flame is simulated with an OpenFOAM®-based CFD code, utilizing the Euler–Lagrange framework. Iron microparticles are modeled as point particles according to the particle-source-in-cell approach. For the gas phase, the usual governing equations for mass, momentum, enthalpy, and chemical species read:

$$\frac{\partial}{\partial t}\rho_\mathrm{g} + \frac{\partial}{\partial x_i}\left(\rho u_{\mathrm{g},i}\right) = S_{\mathrm{prt},m}, \tag{1}$$

$$\frac{\partial}{\partial t}\left(\rho_\mathrm{g} u_{\mathrm{g},i}\right) + \frac{\partial}{\partial x_j}\left(\rho_\mathrm{g} u_{\mathrm{g},i} u_{\mathrm{g},j}\right) = -\frac{\partial}{\partial x_i}p + \frac{\partial}{\partial x_j}\tau_{ij} + \rho_\mathrm{g} g_i + S_{\mathrm{prt},u_{\mathrm{g},i}}, \tag{2}$$

$$\frac{\partial}{\partial t}(\rho_\mathrm{g} h) + \frac{\partial}{\partial x_j}\left(\rho_\mathrm{g} u_{\mathrm{g},j} h\right) = \rho_\mathrm{g} u_{\mathrm{g},j} g_j - \frac{\partial}{\partial x_j} q_j + S_{\mathrm{prt},h} \tag{3}$$

and

$$\frac{\partial}{\partial t}\left(\rho_\mathrm{g} Y_{\mathrm{g},k}\right) + \frac{\partial}{\partial x_j}\left(\rho_\mathrm{g} u_{\mathrm{g},j} Y_{\mathrm{g},k}\right) = \frac{\partial}{\partial x_j}\left(\rho_\mathrm{g} D_k \frac{\partial}{\partial x_j} Y_{\mathrm{g},k}\right) + S_{\mathrm{prt},Y_{\mathrm{g},k}}, \tag{4}$$

where ρ_g is the density, $u_{\mathrm{g},i}$ is the flow velocity in spatial dimension x_i, p is the pressure, τ_{ij} is the stress tensor, g_i is the gravity, h is the enthalpy, q_i is the heat flux, $Y_{\mathrm{g},k}$ is the mass fraction and D_k is the diffusivity of species k. Finally, in the above equations, S_prt represents exchange terms between the continuous gas and the dispersed solid phase, which are defined later.

3.2. Particle model

We use a particle model based on the work of Soo et al. [15,39], which is adapted to iron powder by Hazenberg and van Oijen [6] and later applied to one-dimensional polydisperse iron–air flames by Mich et al. [23] and Ravi et al. [22]. Mich et al. [23] extended the particle model with thermodynamic properties that depend on temperature, which is the framework utilized in this article. In this model, the evolution of the particle mass is given by

$$\frac{\mathrm{d}m_\mathrm{p}}{\mathrm{d}t} = \dot{m}_\mathrm{ox} \tag{5}$$

and that of the iron mass by

$$\frac{\mathrm{d}m_{\mathrm{p,Fe}}}{\mathrm{d}t} = -\frac{1}{s}\dot{m}_\mathrm{ox}, \tag{6}$$

where $\dot{m}_\mathrm{ox}$ is the oxidation rate of the particle and s is the stoichiometric ratio of iron to oxygen. s is given by $M_\mathrm{Fe}/M_{\mathrm{O}_2} = 55.85/15.99$ when complete oxidation up to FeO is assumed and higher oxides are neglected [6]. The particle oxidation rate can be controlled by surface kinetics,

$$\dot{m}_{\mathrm{O}_2,\mathrm{kin}} = \rho_\mathrm{s} Y_{\mathrm{s},\mathrm{O}_2} A_\mathrm{p} k_\infty \exp\left(\frac{-T_\mathrm{a}}{T_\mathrm{p}}\right), \tag{7}$$

or the diffusion of oxygen through the boundary layer (including Stefan flow),

$$\dot{m}_{\mathrm{O}_2,\mathrm{diff}} = -A_\mathrm{p}\frac{Sh\left(\rho D_{\mathrm{O}_2}\right)_\mathrm{f}}{d_\mathrm{p}}\ln\left(1+B_\mathrm{m}\right). \tag{8}$$

In the above equations, Y_{O_2} is the mass fraction of oxygen, A_p is the particle surface area, d_p is the particle diameter, k_∞ is the pre-exponential factor of the surface reaction rate, T_a is the surface reaction activation temperature, Sh is the Sherwood number, $(\rho D_{\mathrm{O}_2})_\mathrm{f}$ is the diffusivity of oxygen inside the film layer and B_m is the Spalding number given by:

$$B_\mathrm{m} = \frac{Y_{\mathrm{s},\mathrm{O}_2} - Y_{\mathrm{g},\mathrm{O}_2}}{1 - Y_{\mathrm{s},\mathrm{O}_2}}. \tag{9}$$

Subscripts $_\mathrm{s}$, $_\mathrm{f}$ and $_\mathrm{g}$ indicate evaluated at the surface, inside the boundary layer and in the bulk gas phase. The overall oxidation rate of a particle is computed by assuming a steady-state boundary layer, such that

$$\dot{m}_\mathrm{kin} = \dot{m}_\mathrm{diff}, \tag{10}$$

which introduces an algebraic relation for $Y_{\mathrm{s},\mathrm{O}_2}$. In our numerical solver, we approximated Eq. (8) by a second-order polynomial function, such that no iterative scheme is required to solve for $Y_{\mathrm{s},\mathrm{O}_2}$, see Supplementary Materials for more details. The mass, volume, and surface area of a particle can be related by assuming that the particle is spherical and the particle density (ρ_p) follows the following simple mixing rule

$$\frac{1}{\rho_\mathrm{p}} = \frac{Y_{\mathrm{p,Fe}}}{\rho_\mathrm{Fe}} + \frac{Y_{\mathrm{p,FeO}}}{\rho_\mathrm{FeO}}, \tag{11}$$

where $Y_{\mathrm{p},i}$ are the species mass fractions inside the particle, and ρ_i are the temperature-dependent densities of Fe and FeO.

The evolution of the particle temperature is described by a temperature equation,

$$m_\mathrm{p} c_\mathrm{p,p}\frac{\mathrm{d}T_\mathrm{p}}{\mathrm{d}t} = \dot{q}_\mathrm{conv} + \dot{q}_\mathrm{rad} + \dot{q}_\mathrm{reac} + \dot{m}_{\mathrm{O}_2} h_{\mathrm{s},\mathrm{O}_2}, \tag{12}$$

where $c_\mathrm{p,p}$ is particle heat capacity, including the latent heat of phase changes, and the right-hand side includes convective heat transport, radiative heat loss, heat of reaction and energy transfer due to enthalpy

transport. For the energy transfer due to enthalpy transport, the enthalpy of oxygen evaluated at the particle surface temperature is used (h_{s,O_2}). In the Supplementary Material we have added the derivation of the temperature equation from the enthalpy equation presented in earlier works, e.g., [6,16,21–23]. The convective heat transfer includes a correction for the Stefan flow and is provided by

$$\dot{q}_{\text{conv}} = -A_{\text{p}} \frac{Nu\lambda_{\text{f}}}{d_{\text{p}}} \left(T_{\text{p}} - T_{\text{g}}\right) \frac{\ln\left(1+B_{\text{t}}\right)}{B_{\text{t}}}, \tag{13}$$

the radiative heat loss is given by

$$\dot{q}_{\text{rad}} = -\epsilon_{\text{p}} \sigma A_{\text{p}} \left(T_{\text{p}}^4 - T_{\text{env}}^4\right), \tag{14}$$

and the heat release of reaction by

$$\dot{q}_{\text{reac}} = -h_{\text{Fe}} \frac{\text{d}m_{\text{p,Fe}}}{\text{d}t} - h_{\text{FeO}} \frac{\text{d}m_{\text{p,FeO}}}{\text{d}t}, \tag{15}$$

where B_{t} is Spalding heat transfer number, Nu is the Nusselt number, ϵ_{p} is the emissivity of the particle, T_{env} is the environment temperature (300K) and σ is the Stefan–Boltzmann constant. In the boundary layer, it is assumed that the Lewis number is unity, i.e., $B_{\text{t}} = B_{\text{m}}$, and the flow is stationary, i.e., $Sh = Nu = 2$. As is conventional when using a temperature equation, Eq. (15) is due to both chemical and sensible changes in enthalpy [40]. Finally, the particle thermodynamics (phase densities, heat capacities, etc.) are described with correlations from the NIST database [41], including transitions between phases.

The OpenFOAM®libraries handle particle tracking; the evolution of the particle velocity is described by

$$m_{\text{p}} \frac{\text{d}u_{\text{p},i}}{\text{d}t} = m_{\text{p}} g_i + F_{\text{d},i} + \left(u_{\text{g},i} - u_{\text{p},i}\right) \frac{\text{d}m_{\text{p}}}{\text{d}t}, \tag{16}$$

the last term is due to the change in particle momentum as a result of the mass change, and $F_{\text{d},i}$ is the drag force provided by

$$F_{\text{d},i} = \frac{1}{2} \rho_{\text{g}} \left|u_{\text{g},i} - u_{\text{p},i}\right| \left(u_{\text{g},i} - u_{\text{p},i}\right) C_{\text{d}} A_{\text{p,c}}, \tag{17}$$

with

$$C_{\text{d}} = \frac{24}{Re_{\text{p},i}} \left(1 + \frac{1}{6} Re_{\text{p},i}^{2/3}\right), \tag{18}$$

where $A_{\text{p,c}}$ the cross-sectional area and Re_{p} the particle Reynolds number.

Based on Eqs. (5), (16) and (12), the exchange terms for a numerical cell with the gas phase are defined as

$$S_{\text{prt},m} = -\frac{1}{V_{\text{cell}}} \sum_m \left(\frac{\text{d}m_{\text{p}}}{\text{d}t}\right)_j n_j, \tag{19}$$

$$S_{\text{prt},u_i} = -\frac{1}{V_{\text{cell}}} \sum_m \left(F_{\text{d},i}\right)_j n_j, \tag{20}$$

$$S_{\text{prt},h} = -\frac{1}{V_{\text{cell}}} \sum_m \left(\dot{q}_{\text{conv}} + h_{\text{O}_2,\text{s}} \frac{\text{d}m_{\text{p}}}{\text{d}t}\right)_j n_j, \tag{21}$$

$$S_{\text{prt},Y_{\text{O}_2}} = -\frac{1}{V_{\text{cell}}} \sum_m \left(\frac{\text{d}m_{\text{p}}}{\text{d}t}\right)_j n_j \tag{22}$$

and

$$S_{\text{prt},i\neq \text{O}_2} = 0, \tag{23}$$

where V_{cell} is the volume of the corresponding cell, the subscript m represents the parcels inside a cell, subscript j is the index of the j'th parcel and n_j is the number of particles per parcel for the j'th parcel.

3.3. Numerical setup

The three-dimensional computational domain for the Bunsen flame is indicated in Fig. 1. It is discretized with 1.1 million cells with inlets for the main pipe flow (particles + air) and co-flow (air) at the bottom of the domain. Only the top 4 mm of the combustion tube and co-flow are included in the numerical domain. The domain then extends for 8 cm above the combustion tubes, easily containing the entire flame, which is around 20 mm high. The co-flow has a radius of 29.4 mm and has a uniform velocity of only air assigned to it at the mean velocity of the combustion tube flow. In the critical region where the flame is located, a radius of 10.25 mm over the entire height of the domain, the cell size is roughly 600 µm. This is larger than the inter-parcel distance, as such the particle boundary layers are not resolved, which is in line with point-particle-in-cell requirements. At the same time, it is sufficiently fine that the flow is stable, and the flame structure is resolved. To validate this, the simulation at $\phi_{\text{Fe}_2\text{O}_3} = 1.0$ and $\bar{v} = 25$ cm/s (see later sections for more details) is also conducted at double the mesh resolution, for which integral values, i.e., extracted burning velocity, changed by at most 5 %. The outlets are located at the sides and top of the domain; a small part of the inlet pipe is included in the model to which no-slip wall boundary conditions are applied. An overview of the boundary conditions is provided in Table 1.

The convection scheme for velocity is set to second order "linear", while for all other equations it is set to first/second order "linearLimited". Time discretization is performed with second order backward difference formula. For the particle equations, the gas phase velocity is interpolated to the particle position, while for the other equation the local cell value is utilized. This combination of schemes provides a good balance between accuracy and stability.

The particle size distribution of the powder utilized in the experiments of Fedoryk et al. [9] is measured both in-situ and with a Camsizer. We believe that the particle size distribution characterized by a Camsizer is more reliable than the in-situ measurements in the article, as it does not depend on the flow conditions of the gas inside the Bunsen setup. Using the Camsizer, three measurements are made of the particle size distribution, each with a different definition of the particle size. The average of the three distributions is taken to which a log-hyperbolic [38] distribution is fitted with satisfactory accuracy (adj. $R^2 = 0.99$), see Fig. 2.

Table 1
Boundary conditions specified for the computational domain.

Surface	T	U	p
Fuel	fixed value	fixed value	fixed value
Co-flow	fixed value	fixed value	zero gradient
Wall	fixed value	no slip	zero gradient
Surroundings	zero gradient	inlet/outlet	wave transmissive

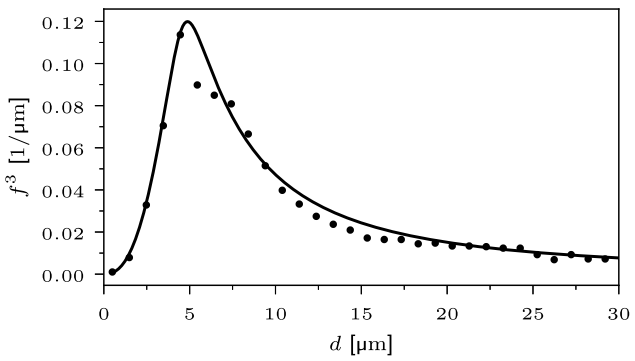

Fig. 2. The experimental particle size distribution and the fitted particle size distribution. f^3 indicates the mass-based particle size probability density function.

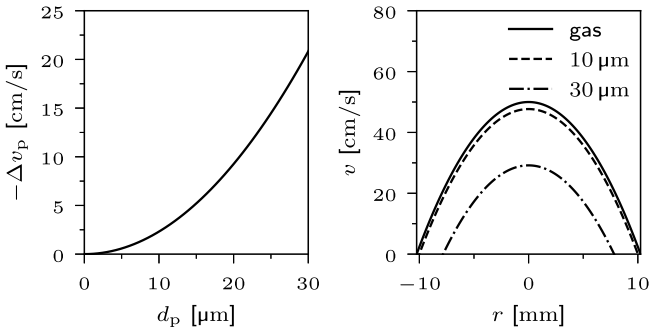

Fig. 3. Left: the terminal slip velocity of the particles as a function of their initial diameter. Right: The inlet velocity profile for the gas and various particle sizes. Particles with negative velocity at the inlet are removed from the simulation.

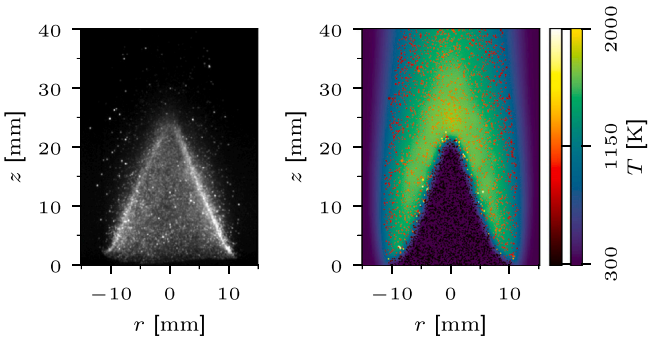

Fig. 4. Comparison between the experimental iron Bunsen flame and the numerical result, at $\bar{v}_{in} = 25$ cm/s and $\phi_{Fe_2O_3} = 1.0$. Left: an image of an instantaneous snapshot of the flame is shown. Right: A slice of the numerical domain showing gas and particle temperatures. The color bar for the particles has been clipped to 2000 K to provide reasonable color resolution in the post-flame zone. (For interpretation of the references to colour in this figure legend, the reader is referred to the web version of this article.)

Only particles between 0.5 and 30 μm are included in the simulation; the distribution is renormalized accordingly. In the Supplementary Material, we provide the particle size distributions, more details on the particle size definitions, and details on the utilized particle size distribution.

The inlet at the central pipe is modeled with a fully developed pipe flow close to the experimentally observed inlet velocity profile [9]. Accordingly, at the inlet, the particles are injected at the terminal velocity, i.e., $F_{d,i} = m_p g_i$, and particles whose velocity is negative at the inlet are removed, see Fig. 3 for reference. We assume that the concentration of the particles above the inlet is uniform, such that the mass flux of particles varies as a function of radius from the inlet center together with the inlet velocity. The local mass flux of the particles is scaled such that the target particle loading is reached if the particle and gas velocities are equal.

Finally, parcels are used instead of particles to reduce the computational load. The smallest parcels (0.5 μm) contain around 2000 particles, and any parcel larger than 6 μm is modeled as a single particle. In between 0.5 and 6 μm, the number of particles per parcel is chosen such that the total initial mass of the particles inside a particle is equal to that of a 6 μm particle. As a result of these settings, the domain contains over 3 million parcels when the flame has reached a (quasi-)steady state. These parcel settings provide a good compromise between accuracy and computational costs.

4. Results

The numerical simulations presented in this article are performed at four of the conditions presented in Fedoryk et al. [9]. Two different equivalence ratios are presented based on Fe_2O_3 as final product, $\phi_{Fe_2O_3} = 1.0$ and 1.5, and two different average inlet velocities $\bar{v_{in}} = 25$ and 40 cm/s. A steady-state flame was obtained and then sampled at 100 Hz for half a second for all the simulations conducted. These time-dependent results show that the flame remains highly stable and cylindrical symmetric; as such, we will not show time-averaged or time-dependent behavior, as this did not modify the results. In this section, we will first visually compare the simulation results against the experiments; second, we will analyze the numerical burning velocity like the experimental flame; third, the flame structure will be compared against 1D numerical results. Finally, the burning velocities of the 3D simulations, 1D simulations and experiments are compared.

4.1. Analysis of the experiments

In Fig. 4, a visual comparison is made between the experimental and numerical result at $\phi_{Fe_2O_3} = 1.0$ and $\bar{v} = 25$ cm/s. From the experiment, an instantaneous snapshot is shown, while the gas-phase and particle temperatures are shown for the numerical results. The snapshot of the experiments presented here has slightly different dimensions than Fig. 4 presented in Fedoryk et al. [9] due to a scaling error in Fig. 4 in their work. This scaling error only affects the z-axis representation in the figure and does not impact the results, as they are based on the original data. The overall shape of the flame in the numerical result is comparable to that of the experimental result. At first sight, the experimental flame appears slightly larger (±25 mm) than the numerical flame (±22.5 mm). However, we should be careful drawing conclusions from these images as two related but different quantities are compared. In the experiment, a line-of-sight measurement is taken from the radiating iron particles. In the numerical result, a contour of the gas temperature and a scatter of the particles sized by their diameter and colored by temperature are shown. It is hard to make a direct comparison, as the experiment shows light intensity from the radiating particles, and the numerical result shows the contours of the gas temperature. Thus, further analysis is required to compare the experimental and numerical results reasonably.

To better compare the numerical results to the experimental results, the laminar burning velocity is estimated from the simulations. For this, three different methods are applied: (1) The area of an iso-contour of temperature $A_{ref}^{T^*}$ is compared with the area of the fuel inlet (A_{in}). The global laminar burning velocity can then be obtained from

$$S_{L,A} = \bar{v_{in}} \frac{A_{in}}{A_{ref}^{T^*}}. \tag{24}$$

(2) The flame front is reconstructed from a temperature iso-contour at T^*. The reconstructed flame front is utilized to obtain the local flame angle ($\theta(r)$). This local flame angle can be compared against the inlet velocity ($v_{in}(r)$) at the same radius. The local flame speed can then be obtained from

$$S_{L,\theta} = v_{in}(r) \cos(\theta(r)). \tag{25}$$

This method was also utilized in the experiments. (3) The same reconstructed flame front as in (2) is utilized to construct a local flame-attached coordinate system. The local velocity vector is then transformed onto this flame-attached coordinate system to obtain the flame-normal (v_η) and flame-tangential (v_ξ) velocity. To obtain the laminar burning velocity, the flame-normal velocity is corrected for gas expansion via a temperature correction, i.e.,

$$S_{L,\eta} = v_\eta \frac{T^*}{T_{in}}. \tag{26}$$

For this third method, care should be taken that the iso-contour of temperature is sufficiently low, such that no oxygen has been transferred from the gas phase to the particles. From methods 2 and 3, an overall laminar burning velocity is obtained by taking the average between

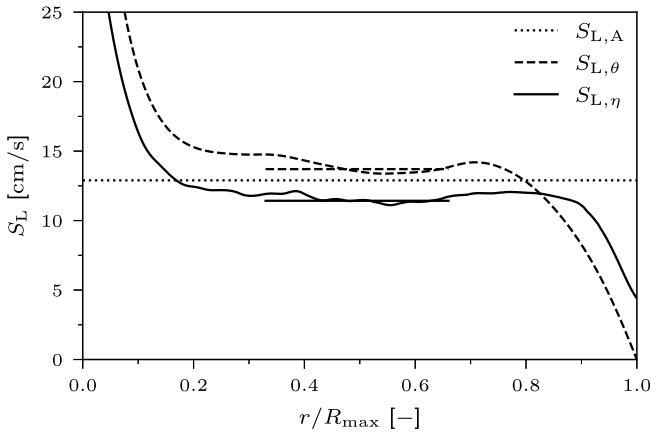

Fig. 5. The laminar burning velocity is estimated from the numerical results of the Bunsen flame using three methods (Eqs. (24)–(26)). The area-based method only provides an overall burning velocity and is thus represented by a constant line. For both the angle and flow method, two lines are shown: a non-constant line, showing the local value, and a constant line between $r/R_{max} = 0.33$ and 0.66, showing the overall burning velocity.

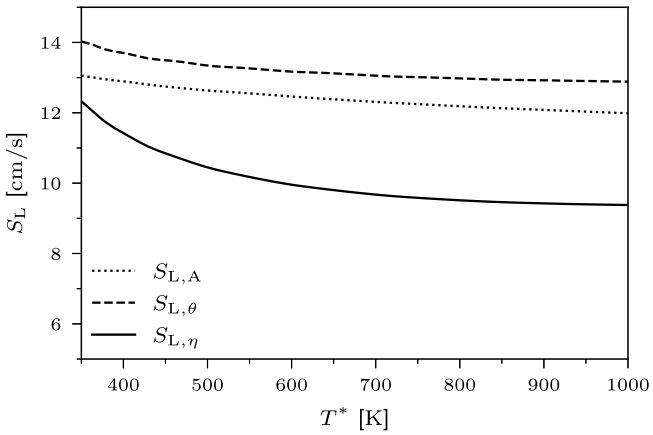

Fig. 6. Dependency of the global laminar burning velocity on the chosen temperature iso-contour. See Fig. 5 for local laminar burning velocity dependency on position.

$r/R_{max} = 0.33$ and 0.66. In all three methods, we assume that the flame is cylindrically symmetric, such that circumferential averaging can be performed. We will refer to method (1) as the area based method, to method (2) as the angle method and to method (3) as the flow method.

The burning velocity is computed using the above three methods for the $\phi = 1.0$ and $\bar{v} = 25$ cm/s case. Results from this computation, utilizing the $T^* = 400$K iso-contour, are depicted in Fig. 5. The graph shows the local burning velocity using the angle and flow method and the global burning velocity of all three methods as a constant line. For the locally computed burning velocity, the trend is similar to what is observed in the experiments (Fig. 6 of Fedoryk et al. [9]): The maximum burning velocity in the center of the Bunsen flame is higher due to the strong curvature of the flame tip, and near the burner rim it tends to zero due to heat loss to the rim. Between $r/R_{max} = 0.33$ and 0.66, the obtained burning velocity varies by less than 1.5 cm/s for both methods. Finally, the burning velocity obtained with all methods is slightly lower than the experimentally observed burning velocity (12.5–15.2 cm/s). This comparison of the burning velocity shows that care must be taken with a simple visual comparison, as in Fig. 4, from which one would conclude that the burning velocity in the numerical simulation is higher than in the experiment.

In Fig. 5, the utilized iso-contour of temperature is an arbitrary choice. As Fedoryk et al. used the optical emission of the radiating particle, a higher iso-contour of temperature is likely much more representative. As such, we have analyzed the impact of the utilized temperature iso-contour on the obtained global burning velocity. In Fig. 6, the iso-contour of temperature varies from 350–1000K, and the global burning velocity using all three methods is computed for each. The graph shows that the obtained burning velocity decreases with increasing temperature iso-contour. In the case of the area and angle method, this decrease is relatively small, around 1 cm/s over the entire range. However, the local flow method shows a more significant decrease of around 3 cm/s. This decrease can be readily explained for the area and angle methods: The temperature iso-contour becomes slightly larger/grows radially outward for increasing temperature. As such, the area increases for the area-based method, while for the angle-based method $v_{in}(r)$ decreases for larger radial coordinates.

For the flow-based method, several effects are at play: As the inlet velocity profile is quadratic (fully developed pipe flow), the flame exhibits both areas of negative stretch for small r/R_{max} and positive stretch for large r/R_{max}, see e.g., [42]. In regions of positive stretch, one would expect that the flame speed obtained by Eq. (26) would decrease, as there is a net mass loss in the local flamelets, while in regions of negative stretch, the reverse would be true. At the same time, as the iso-contour of temperature is increased, the radius of this contour also increases. As a result, after correcting for temperature, the flow velocity must decrease within a flamelet to adhere to conservation, which is not accounted for in Eq. (26). Besides, curvature and stretch can also directly impact the mass burning rate. The impact of either on the mass burning rate has not been studied extensively. The influence of stretch on the burning velocity has been investigated by van Gool et al. [24]; they found that the burning velocity is increased by positive stretch. Further analysis on each of these effects is not performed, as understanding how to extract best a stretch and curvature-free burning velocity from a Bunsen flame is outside the scope of this article.

The global burning velocity of the three other cases simulated will be compared later against the measured burning velocity and 1D results. Based on this single comparison, we conclude that the numerical results show good agreement with the experimental results, or at least they do not show the typical factor of two lower compared to earlier comparisons [6,26]. This agreement provides some validation of the models that have been developed for iron dust flames in recent years.

4.2. Structures of 1D flames

For future comparisons, it is important to understand how well results from the experimental Bunsen flame can be compared to idealized 1D flames. To investigate how well the experimental Bunsen flame compares to a 1D flame, a 1D flamelet is extracted from the 3D Bunsen flame. This extracted flame is then compared against a 1D flame in similar conditions. The flamelet is extracted from the Bunsen flame by reconstructing the flame front, as shown in the right frame of Fig. 7. Identical to the analysis in the previous section, the flame front is reconstructed via the iso-contour of temperature. Given this iso-contour, a local flame coordinate system can be defined at any position along the flame front. The outward pointing direction, from here referred to as η, of this coordinate frame is considered to be a suitable flamelet. In this manner, we have extracted a line at the position $r/R_{max} = 0.5$, the solid line in the right frame of Fig. 7.

Presenting the particle data on a line graph as a function of η provides a challenge, as the particles are discrete. A Gaussian kernel is utilized to convert the particle point data to a line graph. This Gaussian kernel averages (and smooths) the particle data in a small region around a position among the flamelets. The utilized Gaussian kernel has a standard deviation of $\sigma = 0.5\sqrt{2}$mm, and points further away than 1 mm are excluded from the stencil. As particles of various sizes behave very differently, the Gaussian kernel is applied to three bins of particles: b^1 ranges from

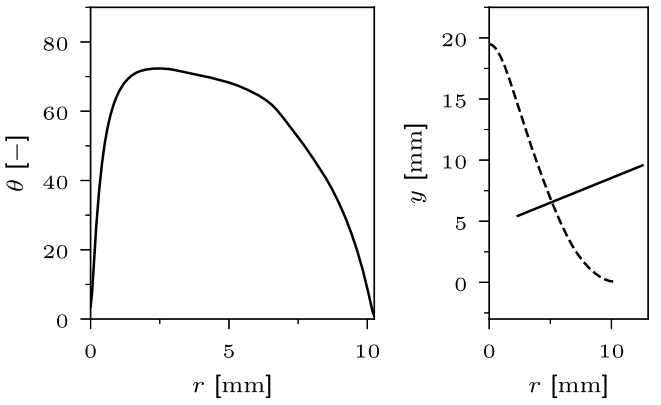

Fig. 7. In the left frame, the local angle of the reconstructed flame with respect to the upward direction is shown. In the right frame, the reconstructed flame front is shown (based on the 400K iso-contour). A local flamelet is drawn, at $r/R_{max} = 0.5$, orthogonal to the temperature iso-contour.

0.5 to 2.5 μm, b^2 ranges from 10 to 15 μm, and b^3 ranges from 20 to 30 μm. The gas phase is also smoothed with the same Gaussian kernel to ensure the relative widths of features in the gas and particle phases are conserved.

To conduct a 1D simulation at a representative condition, the gravity is reduced to account for the angle of the flame front. The angle of the flame front as a function of r is shown in the left frame of Fig. 7. Note that this is the same angle used before in the angle method. The flanks of the Bunsen flame are relatively straight, so the angle is nearly constant (roughly 70 degrees). Based on this, we conduct 1D simulations with a gravity of $g = -9.81\cos(70)$ m/s^2. The data of the 1D flames is then post-processed identically to the 3D flames to provide a fair comparison.

In Fig. 8, the temperature profiles of a 3D flame are compared against the 1D flame. The smallest bin of particles appears to follow the gas phase closely and not significantly exceed it. Unfortunately, this is an unavoidable side effect of the post-processing. The utilized Gaussian kernel removes features that are much smaller than the stencil size. Small particles have very short characteristic time scales, and thus, small features in a spatial sense; the kernel removes these features. The result is that the graphed particle temperature closely follows the gas phase temperature. Moreover, the binning of the particles also removes some features.

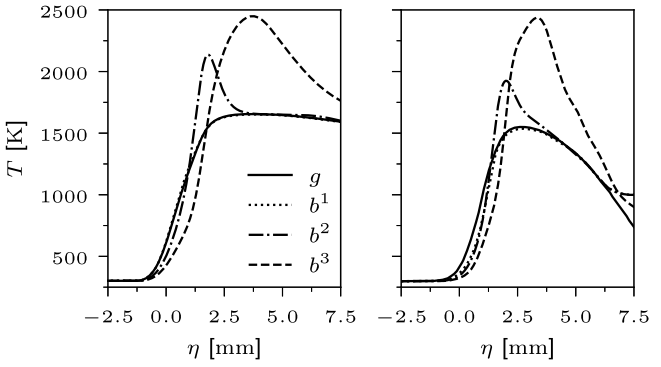

Fig. 8. In the left frame, the temperatures are obtained from a 1D flame simulation. In the right frame, the temperature profile among a flamelet retrieved from the 3D simulation; see Fig. 7 for the position. The particle temperature is post-processed by binning them: b^1 ranges from 0.5 to 2.5 μm, b^2 ranges from 10 to 15 μm, and b^3 ranges from 20 to 30 μm, and the solid lines gives the gas temperature. Smoothing using a Gaussian kernel is applied to both gas and particle temperature profiles for both the 1D and 3D results.

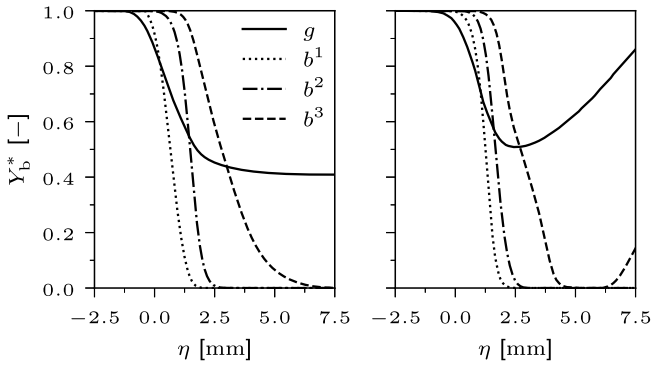

Fig. 9. In the left frame, the unburned fraction profile is obtained from a 1D flame simulation. In the right frame, the unburned fraction profile among a flamelet retrieved from the 3D simulation; see Fig. 7 for the position. The unburned fraction of the gas phase is the normalized oxygen mass fraction, which is presented by the solid line. The particle unburned fraction (Y_{Fe}), is shown by binning them, b^1 ranges from 0.5 to 2.5 μm, b^2 ranges from 10 to 15 μm, and b^3 ranges from 20 to 30 μm. Smoothing using a Gaussian kernel is applied to both gas and particle unburned fraction profiles for both the 1D and 3D results.

Several observations can be made when comparing the 1D and the 3D results. First, the width of the flame front is relatively similar; both fronts start at around $\eta = 0$ mm and end at roughly $\eta = 2.5$ mm. Second, the maximum gas temperature achieved in both flames is roughly 1500K; the 1D simulation provides a slightly higher temperature, and the 3D simulation slightly lower. Third, the position at which bins 2 and 3 achieve the maximum and the maximum temperatures are very similar for 1D and 3D. Finally, in the post-flame zone $\eta > 2.5$ mm, the temperature of the gas phase and the particles reduce much more quickly in the 3D simulation. From observations one to three, we conclude that the flame front of the 3D flame behaves relatively well as a 1D, as the differences for $\eta < 2.5$ mm are minor. However, the post-flame region is not accurately described by the 1D model, as the gas temperature reduces much quicker in the 3D result. If we return to Fig. 7 and look at the solid line representing the extracted flamelet, it can be observed that this line extends beyond $r = R_{max} = 10.25$ mm. This position lies in the cold gas of the co-flow, see Fig. 4, meaning that the co-flow is rapidly cooling the post-flame zone, explaining the differences between the 1D and 3D result.

Similar to the temperature profile, the unburned fraction profiles are also graphed, see Fig. 9. For the particles, the unburned fraction is taken as the mass fraction of Fe in the particle, and for the gas phase, the normalized (with respect to the inlet) O_2 mass fraction is used. Again, several observations can be made comparing the 1D to the 3D result. Until $\eta = 2.5$ mm, the unburned fraction profiles of gas and all particle bins look very similar. The smallest two bins of particles completely combust within this distance, and the distance required to achieve this combustion is very similar. Moreover, the normalized oxygen mass fraction reduces to roughly 0.5. However, the largest bin has barely started burning, so no significant differences can be observed. Beyond $\eta = 2.5$ mm, large differences are present; the gas phase normalized oxygen profile starts to increase again, and the unburned fraction of the largest particles reduces much more quickly. Similar to the temperature profiles, this is oxygen from the co-flow diffusing into the unburned mixture.

To better demonstrate the impact of the co-flow on the extracted 1D profiles, Fig. 10 is provided. In the left frame, the gas phase temperature is shown for the flamelet at three radial positions, $r = 0.33R_{max}$, $0.5R_{max}$ and $0.66R_{max}$. As the radius from which the 1D flame is extracted increases, both the peak gas temperature reduces and the cooling rate in the post-flame zone increases. Below $r = 0.5R_{max}$, the gas phase temperature profile within the flame front is not altered significantly, while

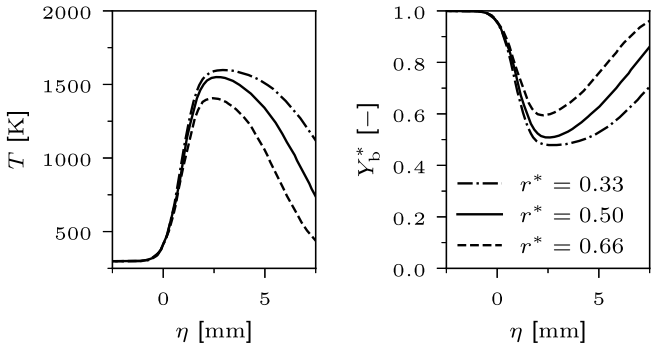

Fig. 10. Gas-phase temperature (left) and unburned fraction (right) profiles are shown. Each profile crosses the temperature iso-contour at a different position ($r* = r/R_{max}$, with r the intersection with the iso-contour) of the reconstructed Bunsen flame.

for larger r, it is modified. Similar observations can be made for the unburned fraction profiles in the right frame, except that the minimum of Y_b^* increases for increasing r, and the rate at which Y_b^* increases reduces. Both the temperature profile and the unburned fraction profile align with our earlier observation: As the radial position of the 1D flame is increased, it is influenced stronger by the cold and oxygen-containing co-flow. Especially for $r > 0.66R_{max}$, a significant portion of the particles combust in an environment that contains more oxygen than the idealized 1D flame, see the left frame of Fig. 9 and compare to the right frame of Fig. 10. One could expect that this increases the burning velocity, as these flames are known to be sensitive to the oxygen concentration and much less to the gas-temperature due to the diffusion-limited combustion of the particles [4]. Based on this observation, the fact that the burning velocity remains nearly constant between $r/R_{max} = 0.3$ and 0.7 in Fig. 5 is surprising. The constant burning velocity suggests that other effects, like varying stretch and curvature, also impact the burning velocity.

Finally, profiles of the velocity normal to the flame front are also compared between the 1D and 3D, see Fig. 11. When comparing the 1D to the 3D results, several observations can be made. First, the laminar burning velocity of the 1D flame is lower than that of the 3D flame. Second, the slip velocity between the various particle bins and the gas phase is similar. Third, the apparent gas expansion of the gas phase over the flame front is less in the 3D flame (±15 to ±45 cm/s, i.e., a factor of roughly three) than in the 1D flame (±10 to ±50 cm/s, i.e., a factor of roughly five). The last observation is interesting, as it can not be explained by the differences of maximum gas phase temperature; see Fig. 8 and note that the peak temperatures are nearly identical. As such, the difference in the gas expansion suggests that the extracted 1D flame is significantly impacted by curvature and or stretch. Fourth, before the flame front the velocity decreases in the 3D case, while it remains constant in the 1D case. This is because for increasing flame coordinate η, the physical coordinate r also increases, see Fig. 7. As the velocity component in the y direction is quadratic (fully developed pipe flow), the y velocity decreases for increasing r. Accordingly, the projection of the y velocity on the η direction decreases for increasing η, explaining the reduction in velocity.

4.3. Comparison of burning velocities

In this final part, the burning velocity estimated from the 3D simulations is compared against the experimental and 1D results, see Fig. 12 For the 3D results, the burning velocity is obtained using the angle method of Eq. (25). The error bar is due to the uncertainty of the temperature iso-contour, range taken from 325 to 1250K. The, until now not presented, simulation results at 40 cm/s and $\phi_{Fe_2O_3} = 1.0$, and both $\bar{v} = 25$ and 40 cm/s at $\phi_{Fe_2O_3} = 1.5$ are included as well. To enhance readability of the graph, the simulation results are offset on the x-axis. Only the experimental results measured at a mean inlet velocity of 40 cm/s are included in the graph to prevent the graph from becoming cluttered. The recovered burning velocity from the 3D simulation shows one of the best agreements between a model and experiment for iron dust flames. It is undoubtedly much better than earlier presented comparisons between 1D models and experiments, often off by more than a factor of two, as observed by Ramaekers et al. [26]. Just as observed in the experiment by Fedoryk et al. [9], the inlet velocity does not significantly impact the obtained burning velocity.

In contrast to the experiment, we observe a weak dependence of the burning velocity on the particle loading. However, the variation of the burning velocity as a function of $\phi_{Fe_2O_3}$ is far below the experimental uncertainty, and we can thus not expect it to be measured. In line with earlier attempts at 1D to experiment comparison, the 1D simulation significantly under-predicts the laminar burning velocity. We can also provide reasons for the differences based on our analysis of the extracted 1D flames.

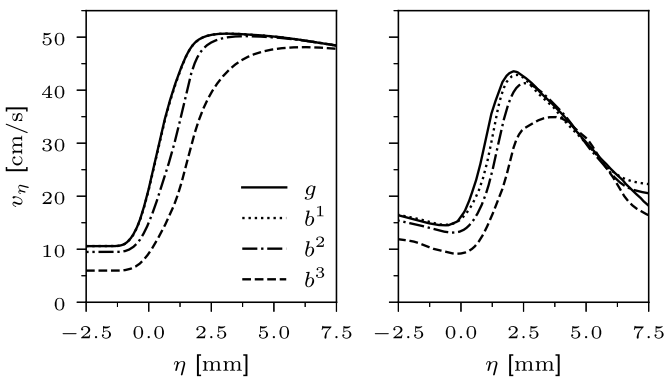

Fig. 11. The velocity profile obtained from a 1D flame simulation is shown in the left frame. In the right frame, the velocity normal to the temperature iso-contour retrieved from the 3D simulation is shown; see Fig. 7 for the position. The particle velocities are shown by binning them: b^1 ranges from 0.5 to 2.5 μm, b^2 ranges from 10 to 15 μm, and b^3 ranges from 20 to 30 μm, and the gas phase velocity is given by the solid line. Smoothing using a Gaussian kernel is applied to both gas and particle velocity profiles for both the 1D and 3D results.

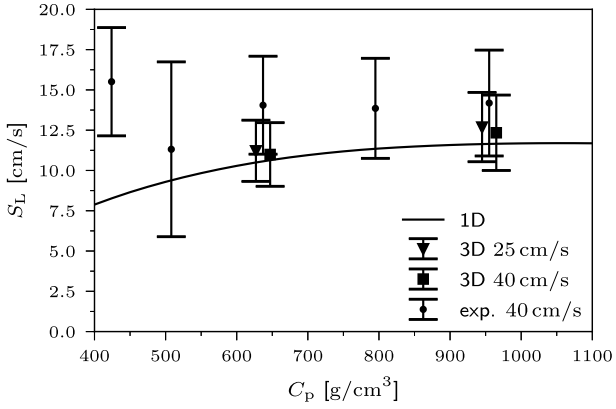

Fig. 12. Comparison of the burning velocity from 1D simulations, 3D Bunsen flame simulations at 25 and 40 cm/s, and experimental results at 40 cm/s. The burning velocity from the 3D simulations is obtained using the angle method Eq. (25) with the 400K iso-contour. The error bars of the 3D simulations is based on the uncertainty due to the temperature iso-contour, see Fig. 6. Results from the 3D simulations are offset on the x-axis to provide readability.

- Oxygen from the co-flow increases the oxygen concentration in the post-flame zone, accelerating the oxidation of large particles.
- Stretch and curvature have some influence on the flame structure.

Only the influence of stretch on the burning velocity has been studied using 1D flames [24], while the impact of curvature or partial premixing has not yet been studied. As such, it is, at this stage, unknown what the relative importance of each of these effects is.

5. Discussion & outlook

In Section 3, the numerical methods are presented as is, without assessment of model assumptions. Here we provide an analysis of limitations in the numerical model and an outlook on how further improvements can be introduced. Some model limitations are unlikely to noticeably impact results at the conditions of the experiments. Still these model limitations are analyzed, in case the community would like to use this model at other conditions. More relevant to this work, limitations in the analysis of the results are discussed as well.

5.1. Model limitations

The model is based on a point particle description for the iron particles. This means that the boundary layer of the particles is modeled with transfer equations, e.g., Eqs. (8), (13) and (17). As a result, if the particle boundary layer cannot be described by these transfer relations the model accuracy suffers. For heterogeneous iron dust flames, this occurs in the discrete regime of flame propagation [43]. While it is still a topic of debate in the community when discrete propagation cannot be neglected [5,29–31], it is accepted that lower particle loading promotes discrete propagation. The $L_\mathrm{p} = \beta d_\mathrm{p}$ parameter from Vance et al. [29,30], with L_p the inter-particle spacing, can be expressed as function of the particle concentration and particle density as

$$\beta = \left(\frac{\pi \rho_\mathrm{p}}{6 C_\mathrm{p}}\right)^{1/3}. \tag{27}$$

The transition from continuous to discrete regime is reported by Vance et al. [30] at $\beta_\mathrm{t} \approx 25$, for lower β the flame behaves continuously. Using the properties for iron, the transition from continuous to discrete occurs at around $C_\mathrm{p} = 250$ g/cm^3. Our simulations at $C_\mathrm{p} \approx 650$ g/cm^3 are thus expected to be well within the continuous regime. However, the leanest case reported by Fedoryk et al. [9] ($\sim$ 425 g/cm^3) is relatively close to the transition regime, which is one of the reasons why we excluded it. The difference between discrete and continuous flames is still at debate, unfortunately, no computationally affordable models exist that can cope with a configuration like the Bunsen setup.

For the oxidation, it is assumed that iron only oxidizes to the first oxide (FeO). This decision was made because oxidation beyond FeO is controlled by thermodynamics [16,17]. van Gool et al. [16], studied this thermodynamically controlled oxidation beyond FeO in flames. They found that oxidation towards higher oxides only occurs after the reaction layer of the flame. This is because the temperature of the iron particles inside the reaction layer is too high for further oxidation. As a result, the burning velocity of an iron–dust flame is mostly controlled by the oxidation to FeO. Except in lean flames ($C_\mathrm{p} < 450$ g/cm^3), for these flames, the additional heat release of the higher oxides significantly affects the flame temperature and thereby the burning velocity. As higher oxides become important when discrete propagation should be considered, we decided not to consider the higher oxides. The exclusion of higher oxides is the main reason that we did not simulate the two leaner cases by Fedoryk et al. [9]. In the future, the model can be extended, which becomes especially important for practical combustors, where there is an interest in the final particle composition.

In the model, we assumed that the conversion rate of a particle is controlled by a first-order surface reaction. This is a simple, easy to interpret, and computationally affordable model. However, Mi et al. [19] developed a more elaborate model based on solid-state diffusion. The physical basis of the model is better than for the first order surface reaction model, and the predicted ignition temperature in air is remarkably close to experimental results [44–46]. But, as most of the oxidation occurs while the rate of reaction is limited by external diffusion (diffusion in the particle boundary layer), the impact of the kinetic model on burning velocity is relatively small [17]. A concern with the model of Mi et al. [19] is that it includes oxidation up to Fe_3O_4 (which in their work is fine, as it focuses on ignition), without considering the previously mentioned thermodynamic constraints. While it would be possible to disable the reaction to Fe_3O_4, we opted to use the simpler first-order surface reaction model in this work. The influence of the ignition model is expected to be in the order of 10 % on the burning velocity. Still, and especially for simulations in more complex burners, a more advanced reaction model in combination with a higher oxide model can be considered.

In the experiments of Fedoryk et al. [9], a fine iron powder is used (a Sauter mean diameter of roughly 7 μm). For such a fine powder, diffusion of oxygen towards the particle surface cannot be accurately modeled by continuum diffusion. In this case, part of the particle boundary layer should be modeled with free-molecular diffusion [47,48]. Free molecular diffusion increases the particle burn time of particles of 7 μm by roughly 20 % or the burning velocity by roughly 10 %, as $S_\mathrm{L} \propto \sqrt{1/\tau_\mathrm{b}}$, with τ_b the burn time. However, the uncertainty of the particle burn time in the transition regime due to model parameters is large [47]. These model parameters can be estimated from molecular dynamics simulations, but the parameters vary widely based on the molecular force field used [49]. As an elaborate model that considers free-molecular diffusion is much more computationally expensive and model parameters are uncertain, we decided to neglect its effect.

In our numerical model, particle-to-particle radiation was neglected, under the assumption that it is negligible. This appears to contradict with Rameakers et al. [26], who find that particle-to-particle radiation can have an impact. The reason for this apparent difference is due to the dimensions of the experimental configuration. Rameakers et al. investigated the experiments performed by Tang et al. [27,34]. An important parameter for estimating the importance of particle-to-particle radiation is the optical path length. When the optical path-length is smaller or comparable to the configuration dimensions, particle-to-particle radiation is likely significant. For a polydisperse powder, this can be estimated from

$$L_\mathrm{opt} = \frac{2\rho_\mathrm{p}}{3 C_\mathrm{p} \epsilon_\mathrm{p} \int_{d_\mathrm{p,min}}^{d_\mathrm{p,max}} \frac{f^3(d_\mathrm{p})}{d_\mathrm{p}} \mathrm{d}d_\mathrm{p}}, \tag{28}$$

where $f^3(d_\mathrm{p})$ is the volume based particle size distribution, see Supplementary Materials for more information. In the experiments of Tang et al. [27,34], the optical path length is 60 % and 135 % of the configuration diameter, for the finest and second-finest powder respectively. Rameakers et al. then find that the finest powder is significantly impacted by particle-to-particle radiation and the second finest weakly. In the experimental configuration of Fedoryk et al. [9] we estimate $L_\mathrm{opt} = 40$ mm at $C_\mathrm{p} = 1000$ g/cm^3. This is twice the diameter of the experimental configuration and, thus, particle-to-particle radiation is negligible. While it is unlikely that the results are significantly modified, it can be worthwhile to verify this.

The Saffman lift force is not included in the forces applied to the particle. If included, particles would experience a lift force towards the center of the combustion tube, due to flow shear. This lift force can redistribute particles on the inlet based on particle size, as the magnitude of the lift force depends on particle size. Over the entire length of the combustion tube, the Saffman lift force is significant. However, as we on only simulate the last 4 mm of the combustion tube, the Saffman lift force is neglected. If the simulation domain is enlarged or more complex flows are simulated it should be included.

5.2. Boundary condition limitations

In the experiments, particle seeding takes place inside the combustion tube, see Fig. 1 for reference. This tube has a length of 35 cm above the pilot tube. To significantly cut back on computational costs, we excluded this tube in our simulations and only consider the last 4 mm and 8 cm above the tube outlet. As mixing of the particles and gas-phase takes place inside the combustion tube, the information about the quality of this mixing is not in the simulations. To overcome this, it is assumed that the mixing is perfect, i.e., the particle density and size distribution do not depend on the radial coordinate. However, even if it is assumed that mixing is ideal at the bottom the aforementioned Saffman lift force would introduce a radial dependency. Moreover, from the experiments [9] we know that small fluctuations in the particle concentration occur. These seeding fluctuations might originate inside the combustion tube. We think that the ideal seeding assumption is a very large source of uncertainty, which should be the focus of future research.

5.3. Limitations in the analysis

Our burning velocity comparison with the experiments is based on a temperature iso-contour, while in the experiments it's based on the Abel inverse of particle radiation. Clearly, these are two rather different quantities, but still related to some extent as radiation scales by temperature to the power of four. The first challenge arises in the transformation of a point cloud of radiating particles to a 2D image. In our, not shown, analysis we tried the simple approach: assume that the camera is infinitely far away and particle emissivity does not depend on temperature or composition. When the camera is far away, all light rays from all particles become parallel, such that every particle is always in focus, and no light absorption by other particles. Strictly, the radiant flux on the camera becomes zero in this case, but a theoretical camera can be infinitely sensitive. In this case, it is easy to reconstruct a numerical photograph of the measurements. Unfortunately, it compared poorly to the photographs provided in Fedoryk et al. [9]. This is likely because light rays are not parallel, light from the back of the Bunsen flame is absorbed by particles at the front, overexposure of pixels leads to leakage to neighbors, particles within a parcel are not jittered, and the emissivity of the particle depends on composition. To resolve the non-parallel light rays, light absorption and jittering of particles within a parcel, a Monte Carlo path tracing can be employed, which is computationally expensive and would introduce new fitting parameters (e.g., aperture size, lens size, distance to Bunsen flame, etc.). Moreover, the dependence of the emissivity on composition/temperature and over exposure effects would have to be estimated. This would introduce an extremely complex analysis, which is far outside the scope of this article, and introduce new unknown parameters. Thus, we opted to keep the analysis easily interpretable and use the iso-contour of the gas-phase temperature instead. The 400K iso-contour was then used to provide results at the unburned side of the flame, which should be close to idealized 1D flames. Many studies are possible to extend this analysis to improve our understanding of how to best extract the burning velocity from these flames. These could include the above "photograph" based analysis, but also analysis based on particle tracking, e.g., [13,50].

6. Conclusion

In this article, we have performed 3D simulations of the experimental setup presented by Fedoryk et al. [9]. With a relatively simple particle model, we have obtained satisfactory agreement between experiment and simulation. This agreement suggests that the missing factor two, observed in several publications, e.g., [6,26,27], is because 3D flames do not translate well into idealized 1D flames. Using our results, we have estimated the burning velocity utilizing three different methods: (1) The burning velocity is obtained from the surface area of the flame, (2) the local angle of the flame front is compared against the inlet velocity, and (3) the local gas velocity normal to a temperature iso-contour. The method based on the local gas velocity is the only one that can account for the impact of the flame front on the flow field just in front of the flame; as such, this method is expected to be the most accurate. However, this requires direct measurement of the gas velocity, as particles experience significant slip, see Fig. 11. Thus, this method might be challenging to utilize in practice. When these three methods are compared, two conclusions can be made: (1) all three methods have some sensitivity to the utilized temperature iso-contour, but the velocity based method is very sensitive, and (2) the angle based method produces the highest burning velocity. When comparing against the experimental results, it is observed that the burning velocity obtained by the angle based method is very close to the measurement values. The angle based method (based on particle radiation) is also utilized in the experiments, and shows minimal sensitivity to the chosen temperature iso-contour, see Fig. 5. The similar method and low sensitivity provide confidence in the quality of the agreement. As discussed in the previous section, still many uncertainties remain about the impact of various model improvements and the interpretation of the experiments. While this provides a validation for using our model for flame propagation, it does not provide validation for other cases, e.g., turbulent flames.

Flame structures are compared to better understand the differences between 1D and 3D burning velocities. From this, we conclude that mixing between the burned gas and the co-flow occurs. This mixing is large enough that some oxygen from the co-flow can diffuse into the reaction layer of the Bunsen flame, very likely enhancing the flame speed. Of course, the cold gas from the co-flow also reduces the flame temperature, but iron dust flames are not very sensitive to the flame temperature, e.g., [6]. Moreover, we also noted that curvature and stretch effects will likely modify the Bunsen flame's laminar burning velocity. It is imperative that the impact of these effects is better understood so that more reliable measurements of the burning velocity can be performed. Further research on (quasi) 1D flames can be used to improve our understanding. For example, using 1D counterflow simulations, e.g., [24], the effect of stretch and partial-premixing of oxygen can be isolated. While curvature has been studied with boundary layer resolved simulations by Vance et al. [31], no model has been developed to study the impact of curvature on the burning velocity in a 1D framework, such a model can prove crucial to help study the influence of curvature on the burning velocity.

CReDiT authorship contribution statement

T. Hazenberg: Conceptualization, Data curation, Formal analysis, Investigation, Methodology, Software, Validation, Visualization, Writing - original draft. **D. Braig:** Conceptualization, Data curation, Formal analysis, Investigation, Methodology, Software, Validation, Writing - reviewing & editing. **M. A. Fedoryk:** Data curation, Validation, Writing - reviewing & editing. **J. Mich:** Software, Validation, Writing - reviewing & editing. **F. P. Hagen:** Project administration, Supervision, Writing - reviewing & editing. **S. R. Harth:** Project administration, Supervision, Writing - reviewing & editing. **B. Stelzner:** Project administration, Supervision, Writing - reviewing & editing. **A. Scholtissek:** Conceptualization, Funding acquisition, Project administration, Supervision, Writing - reviewing & editing. **D. Trimis:** Conceptualization, Funding acquisition, Project administration, Supervision, Writing - reviewing & editing. **C. Hasse:** Conceptualization, Funding acquisition, Project administration, Resources, Supervision, Writing - reviewing & editing.

Declaration of competing interest

The authors declare that they have no known competing financial interests or personal relationships that could have appeared to influence the work reported in this paper.

Acknowledgments

This work was funded by the Hessian Ministry of Higher Education, Research, Science and the Arts - cluster project Clean Circles.

Data availability

Data will be made available on request.

References

[1] Mignard D, Pritchard C. A review of the sponge iron process for the storage and transmission of remotely generated marine energy. Int J Hydrogen Energy 2007;32(18):5039–49. https://doi.org/10.1016/j.ijhydene.2007.06.032.

[2] Bergthorson JM, Goroshin S, Soo MJ, Julien P, Palecka J, Frost DL, et al. Direct combustion of recyclable metal fuels for zero-carbon heat and power. Appl Energy 2015;160:368–82. https://doi.org/10.1016/j.apenergy.2015.09.037.

[3] Bergthorson JM. Recyclable metal fuels for clean and compact zero-carbon power. Prog Energy Combust Sci 2018;68:169–96. https://doi.org/10.1016/j.pecs.2018.05.001.

[4] Goroshin S, Palečka J, Bergthorson JM. Some fundamental aspects of laminar flames in nonvolatile solid fuel suspensions. Prog Energy Combust Sci 2022;91:100994. https://doi.org/10.1016/j.pecs.2022.100994.

[5] Ning D, Shoshin Y. Thermal inertia effect of reactive sources on one-dimensional discrete combustion wave propagation. Combust Flame 2023;253:112790. https://doi.org/10.1016/j.combustflame.2023.112790.

[6] Hazenberg T, van Oijen JA. Structures and burning velocities of flames in iron aerosols. Proc Combust Inst 2021;38(3):4383–90. https://doi.org/10.1016/j.proci.2020.07.058.

[7] McRae M, Julien P, Salvo S, Goroshin S, Frost DL, Bergthorson JM. Stabilized, flat iron flames on a hot counterflow Burner. Proc Combust Inst 2019;37(3):3185–91. https://doi.org/10.1016/j.proci.2018.06.134.

[8] Julien P, Whiteley S, Goroshin S, Soo MJ, Frost DL, Bergthorson JM. Flame structure and particle-combustion regimes in premixed methane-iron-air suspensions. Proc Combust Inst 2015;35(2):2431–38. https://doi.org/10.1016/j.proci.2014.05.003.

[9] Fedoryk M, Stelzner B, Harth S, Trimis D. Experimental investigation of the laminar burning velocity of iron-air flames in a tube Burner. Appl Energy Combust Sci 2023;13:100111. https://doi.org/10.1016/j.jaecs.2022.100111.

[10] Sun J-H, Dobashi R, Hirano T. Structure of flames propagating through metal particle clouds and behavior of particles. Symp (Int) Combust 1998;27(2):2405–11. https://doi.org/10.1016/s0082-0784(98)80092-1.

[11] Sun J-H, Dobashi R, Hirano T. Combustion behavior of iron particles suspended in air. Combust Sci Technol 2000;150(1–6):99–114. https://doi.org/10.1080/00102200008952119.

[12] Hulsbos MR, Hermanns RTE, Bastiaans RJM, de Goey LPH. The heat flux method for hybrid iron-methane-air flames. Combust Flame 2024;266:113531. https://doi.org/10.1016/j.combustflame.2024.113531.

[13] Krenn T, Li T, Hebel J, Böhm B, Dreizler A. Evaluation of a novel measurement method for the laminar burning speed in laminar lifted iron dust flames. Fuel 2024;366:131266. https://doi.org/10.1016/j.fuel.2024.131266.

[14] Baigmohammadi M, Prasidha W, Stevens NC, Shoshyn YL, Spee T, De Goey P. Towards utilization of iron powders for heating and power. Appl Energy Combust Sci 2023;13:100116. https://doi.org/10.1016/j.jaecs.2023.100116.

[15] Soo MJ, Kumashiro K, Goroshin S, Frost DL, Bergthorson JM. Thermal structure and burning velocity of flames in non-volatile fuel suspensions. Proc Combust Inst 2017;36(2):2351–58. https://doi.org/10.1016/j.proci.2016.06.043.

[16] van Gool CEAG, Thijs LC, Ramaekers WJS, van Oijen JA, de Goey LPH. Particle equilibrium composition model for iron dust combustion. Appl Energy Combust Sci 2023;13:100115. https://doi.org/10.1016/j.jaecs.2023.100115.

[17] Mich J, da Silva AK, Ning D, Li T, Raabe D, Böhm B, et al. Modeling the oxidation of iron microparticles during the reactive cooling phase. Proc Combust Inst 2024;40(1–4):105538. https://doi.org/10.1016/j.proci.2024.105538.

[18] Thijs LC, van Gool CEAG, Ramaekers WJS, Kuerten JGM, van Oijen JA, de Goey LPH. Improvement of heat- and mass transfer modeling for single iron particles combustion using resolved simulations. Combust Sci Technol 2022;196(4):572–88. https://doi.org/10.1080/00102202.2022.2089030.

[19] Mi X, Fujinawa A, Bergthorson JM. A quantitative analysis of the ignition characteristics of fine iron particles. Combust Flame 2022;240:112011. https://doi.org/10.1016/j.combustflame.2022.112011.

[20] Goroshin S, Bidabadi M, Lee JHS. Quenching distance of laminar flame in aluminum dust clouds. Combust Flame 1996;105(1–2):147–60. https://doi.org/10.1016/0010-2180(95)00183-2.

[21] Ravi A, Goey PD, Oijen JV. Flame structure and burning velocity of flames propagating in binary iron aerosols. Proc Combust Inst 2023;39(3):3573–81. https://doi.org/10.1016/j.proci.2022.07.031.

[22] Ravi A, Goey PD, Oijen JV. Effect of particle size distribution on the laminar flame speed of iron aerosols. Combust Flame 2023;257:113053. https://doi.org/10.1016/j.combustflame.2023.113053.

[23] Mich J, Braig D, Gustmann T, Hasse C, Scholtissek A. A comparison of mechanistic models for the combustion of iron microparticles and their application to polydisperse iron-air suspensions. Combust Flame 2023;256:112949. https://doi.org/10.1016/j.combustflame.2023.112949.

[24] van Gool CEAG, Hazenberg T, van Oijen JA, de Goey LPH. Numerical determination of iron dust laminar flame speeds with the counter-flow twin-flame technique. Combust Flame 2024;266:113524. https://doi.org/10.1016/j.combustflame.2024.113524.

[25] Wen X, Scholtissek A, van Oijen J, Bergthorson J, Hasse C. Numerical modeling of pulverized iron flames in a multidimensional hot counterflow burner. Combust Flame 2023;248:112572. https://doi.org/10.1016/j.combustflame.2022.112572.

[26] Ramaekers WJS, Hazenberg T, Thijs LC, Roekaerts DJEM, van Oijen JA, de Goey LPH. The influence of radiative heat transfer on flame propagation in dense iron-air aerosols. Combust Flame 2025;272:113848. https://doi.org/10.1016/j.combustflame.2024.113848.

[27] Tang F-D, Goroshin S, Higgins A, Lee J. Flame propagation and quenching in iron dust clouds. Proc Combust Inst 2009;32(2):1905–12. https://doi.org/10.1016/j.proci.2008.05.084.

[28] Tang F-D, Goroshin S, Higgins AJ. Modes of particle combustion in iron dust flames. Proc Combust Inst 2011;33(2):1975–82. https://doi.org/10.1016/j.proci.2010.06.088.

[29] Vance FH, Scholtissek A, Nicolai H, Hasse C. Flame propagation modes for iron particle clusters in air–part I: transition from continuous to discrete propagation mode under weak convection effects. Combust Flame 2024;260:113265. https://doi.org/10.1016/j.combustflame.2023.113265.

[30] Vance FH, Scholtissek A, Nicolai H, Hasse C. Flame propagation modes for iron particle clusters in air, part II: transition from continuous to discrete propagation mode under strong convection effects. Combust Flame 2024;265:113199. https://doi.org/10.1016/j.combustflame.2023.113199.

[31] Vance FH, Scholtissek A, Nicolai H, Hasse C. A numerical analysis of multi-dimensional iron flame propagation using boundary-layer resolved simulations. Fuel 2024;369:131793. https://doi.org/10.1016/j.fuel.2024.131793.

[32] Tang F-D, Higgins AJ, Goroshin S. Effect of discreteness on heterogeneous flames: propagation limits in regular and random particle arrays. Combust Theor Model 2009;13(2):319–41. https://doi.org/10.1080/13647830802632184.

[33] Goroshin S, Tang F-D, Higgins AJ. Reaction-diffusion fronts in media with spatially discrete sources. Phys Rev E 2011;84(2):027301. https://doi.org/10.1103/physreve.84.027301.

[34] Tang F-D, Higgins AJ, Goroshin S. Propagation limits and velocity of reaction-diffusion fronts in a system of discrete random sources. Phys Rev E 2012;85(3):036311. https://doi.org/10.1103/physreve.85.036311.

[35] Ning D, Hazenberg T, Shoshin Y, van Oijen JA, Finotello G, de Goey LPH. Experimental and theoretical study of single iron particle combustion under low-oxygen dilution conditions. Fuel 2024;357:129718. https://doi.org/10.1016/j.fuel.2023.129718.

[36] Thijs LC, Ning D, Shoshin YS, Hazenberg T, Mi X, van Oijen JA, et al. Temperature evolution of laser-ignited micrometric iron particles: a comprehensive experimental data set and numerical assessment of laser heating impact. Appl Energy Combust Sci 2024;19:100284. https://doi.org/10.1016/j.jaecs.2024.100284.

[37] Ning D, Shoshin Y, van Oijen J, Finotello G, de Goey L. Burn time and combustion regime of laser-ignited single iron particle. Combust Flame 2021;230:111424. https://doi.org/10.1016/j.combustflame.2021.111424.

[38] Barndorff-Nielsen O. Exponentially decreasing distributions for the logarithm of particle size, Proc Royal Soc London A Math Phys Sci 1977;353(1674):401–19. https://doi.org/10.1098/rspa.1977.0041.

[39] Soo M, Goroshin S, Bergthorson JM, Frost DL. Reaction of a particle suspension in a rapidly-heated oxidizing gas. Propell Explos Pyrotech 2015;40(4):604–12. https://doi.org/10.1002/prep.201400269.

[40] Poinsot T, Veynante D. Theoretical and numerical combustion. 2nd ed. Philadelphia, Pa: Edwards; 2005. includes bibliographical references (p. 497–518) and index.

[41] Chase MW Jr. NIST-JANAF themochemical tables, fourth edition. J Phys Chem Ref Data 1998;9:1–1951.

[42] Fu J, Tang C, Jin W, Huang Z. Effect of preferential diffusion and flame stretch on flame structure and laminar burning velocity of syngas Bunsen flame using OH-PLIF. Int J Hydrogen Energy 2014;39(23):12187–93. https://doi.org/10.1016/j.ijhydene.2014.06.043.

[43] Goroshin S, Lee JHS, Shoshin Y. Effect of the discrete nature of heat sources on flame propagation in particulate suspensions. Symp (Int) Combust 1998;27(1):743–49. https://doi.org/10.1016/s0082-0784(98)80468-2.

[44] Abdallah M, Shoshin Y, Finotello G, de Goey LPH. Iron particles ignition in different hot coflow temperatures. Proc Combust Inst 2024;40(1–4):105261. https://doi.org/10.1016/j.proci.2024.105261.

[45] Ning D, Li Y, Li T, Böhm B, Dreizler A. Size-resolved ignition temperatures of isolated iron microparticles. Combust Flame 2024;270:113779. https://doi.org/10.1016/j.combustflame.2024.113779.

[46] Cen L, Lyu Z, Qian Y, Zhong W, Lu X. A detailed experimental and numerical study on the ignition temperature of single micron-sized spherical iron particles. Combust Flame 2025;272:113909. https://doi.org/10.1016/j.combustflame.2024.113909.

[47] Thijs LC, Kritikos EM, Giusti A, Ramaekers G, van Oijen JA, de Goey P, et al. On the surface chemisorption of oxidizing fine iron particles: insights gained from molecular dynamics simulations. Combust Flame 2023;254:112871. https://doi.org/10.1016/j.combustflame.2023.112871.

[48] Jean-Philyppe J, Fujinawa A, Bergthorson JM, Mi X. The ignition of fine iron particles in the Knudsen transition regime. Combust Flame 2023;255:112869. https://doi.org/10.1016/j.combustflame.2023.112869.

[49] Thijs LC, Kritikos EM, Giusti A, van Ende M-A, van Duin ACT, Mi X. Effect of Fe-O ReaxFF on liquid iron oxide properties derived from reactive molecular dynamics. J Phys Chem A 2023;127(48):10339–55. https://doi.org/10.1021/acs.jpca.3c06646.

[50] Lomba R, Laboureur P, Dumand C, Chauveau C, Halter F. Determination of aluminum-air burning velocities using PIV and Laser sheet tomography. Proc Combust Inst 2019;37(3):3143–50. https://doi.org/10.1016/j.proci.2018.07.013.